



Pulse imaging and nonadiabatic control of solid-state artificial atoms

Jonas Bylander,^{1,*} Mark S. Rudner,^{2,3} Andrey V. Shytov,⁴ Sergio O. Valenzuela,^{5,†} David M. Berns,^{1,2} Karl K. Berggren,^{6,‡} Leonid S. Levitov,² and William D. Oliver^{1,6}

¹*Research Laboratory of Electronics, Massachusetts Institute of Technology (MIT), 77 Massachusetts Avenue, Cambridge, Massachusetts 02139, USA*

²*Department of Physics, Massachusetts Institute of Technology (MIT), 77 Massachusetts Avenue, Cambridge, Massachusetts 02139, USA*

³*Department of Physics, Harvard University, 17 Oxford Street, Cambridge, Massachusetts 02138, USA*

⁴*Department of Physics, University of Utah, Salt Lake City, Utah 84112, USA*

⁵*Francis Bitter Magnet Laboratory, Massachusetts Institute of Technology (MIT), 77 Massachusetts Avenue, Cambridge, Massachusetts 02139, USA*

⁶*MIT Lincoln Laboratory, 244 Wood Street, Lexington, Massachusetts 02420, USA*

(Received 25 December 2008; published 23 December 2009)

Transitions in an artificial atom, driven nonadiabatically through an energy-level avoided crossing, can be controlled by carefully engineering the driving protocol. We have driven a superconducting persistent-current qubit with a large-amplitude radio-frequency field. By applying a biharmonic wave form generated by a digital source, we demonstrate a mapping between the amplitude and phase of the harmonics produced at the source and those received by the device. This allows us to image the actual wave form at the device. This information is used to engineer a desired time dependence, as confirmed by the detailed comparison with a simulation.

DOI: [10.1103/PhysRevB.80.220506](https://doi.org/10.1103/PhysRevB.80.220506)

PACS number(s): 03.67.Lx, 32.80.Qk, 78.70.Gq, 85.25.Cp

Due to the strong coupling of solid-state artificial atoms^{1,2} to electromagnetic fields, a wide range of pulsing techniques can be used to manipulate and control such systems. A common approach, first developed for natural atomic systems, involves low-frequency Rabi oscillations driven by low-amplitude microwave radiation,^{3–6} combined with envelope-shaping techniques.^{7,8} However, strong driving affords many more possibilities for quantum control. Fast dc pulses can be used to bring the system nonadiabatically into the vicinity of an avoided level crossing, where coherent oscillations result from Larmor-type precession.^{9–11}

Furthermore, quantum coherence was recently shown to persist under large-amplitude harmonic driving.^{12–18} In this regime, by carefully engineering the driving protocol, arbitrary rotations of a qubit's quantum state on the Bloch sphere could be performed.¹⁸ Such protocols may lead to faster quantum-logic gates than typically achieved using Rabi-based techniques, approaching the Larmor precession rate. To make this approach feasible, one must be able to apply external fields of arbitrary time dependence to a quantum device. With this ability, the techniques used for pulsed NMR can be extended to achieve even higher-fidelity quantum control.¹⁹

In addition to the challenge of designing optimized pulses, accurately delivering them to a device in a cryogenic environment is a difficult problem in its own right, especially at radio and microwave frequencies. In particular with transient pulses,^{9–11} it is hard to determine the exact pulse shape at the device. Although digital wave-form generators offer the possibility to create control pulses with essentially arbitrary time dependence, the signal that reaches the device may be strongly distorted due to the impedance mismatch and frequency dispersion that can occur in the long coaxial cables leading from the generator to the device. Thus, in order to achieve high-fidelity quantum control, it is important to learn not only how to design optimized pulses with arbitrary

shape in the computer, but also how to apply them faithfully to the device under study.

In this Rapid Communication we present methods to image the extremal points of a periodic signal and the actual wave form of a single pulse, as received by the device. Applied to digitally generated, radio-frequency biharmonic pulses [Eq. (1)], this approach allows us to determine the amplitude ratio and phase between harmonics, as illustrated in Figs. 1 and 3. Using this information, we create wave forms that are calibrated to accurately produce the desired time dependence at the device. In particular, the ability to engineer wave forms is used to control the time spent near an avoided crossing. The effect of the latter on quantum evolution is illustrated and confirmed by detailed comparison with simulations.

In our experiments, we use a niobium superconducting persistent-current qubit [see Fig. 1(a)]. When the magnetic flux f piercing the qubit loop is nearly $\Phi_0/2$, where $\Phi_0 = h/2e$ is the flux quantum, the qubit's potential energy exhibits a double-well profile. The system then supports a set of discrete diabatic states $\{|p, L\rangle, |q, R\rangle; (p, q) = 0, 1, \dots\}$, localized in the left and right wells, and associated with opposing persistent currents. Their energies vary linearly with the magnetic flux and exhibit avoided level crossings [see Fig. 1(b)].

We drive the system longitudinally with an applied flux $\delta f(t) \equiv f(t) - \Phi_0/2 = \delta f_{dc} + f_{rf}(t)$ consisting of a static and a time-dependent part. This driving creates large-amplitude excursions through the energy-level diagram from the point of the static flux bias δf_{dc} , as indicated by the arrows in Fig. 1(b). The quantum evolution is primarily adiabatic, except when the field sweeps through the energy-level avoided crossings $\Delta_{p,q}$ where Landau-Zener (LZ) transitions split the state into coherent superpositions of $|p, L\rangle$ and $|q, R\rangle$. When the excursion extends over multiple levels, the interplay between LZ transitions at different crossings and intrawell re-

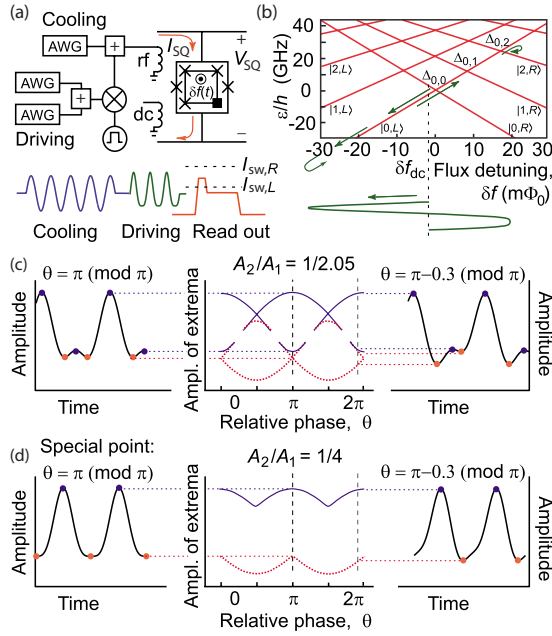


FIG. 1. (Color online) (a) Schematic experimental setup. The device was placed at 20 mK (see Ref. 13 for details). (b) Energy diagram determined by amplitude spectroscopy (Ref. 16). The energy gaps are small on the scale of the figure ($\Delta_{0,q}/h=0.013, 0.090, 0.40$, and 2.2 GHz for $q=0, \dots, 3$, respectively). Below: flux excursion $\delta f(t)$ during the short biharmonic pulse that probes the time-dependent dynamics in Fig. 3. (c),(d) Biharmonic wave-form examples (1). θ values are indicated by dashed vertical lines; solid blue (dotted red) lines denote maxima (minima). The lower left wave form corresponds to the one in Fig. 3(b).

relaxation ($|p', L\rangle \rightarrow |p, L\rangle$ and $|q', R\rangle \rightarrow |q, R\rangle$) gives rise to “spectroscopy diamonds” in the saturated population¹⁶ as shown in Fig. 2(a). Because the LZ-transition probability $P_{LZ}=1-\exp(-\pi\Delta_{p,q}^2/2\hbar v)$ is exponentially sensitive to the energy sweep rate v through the avoided crossing, the magnitude of population transfer contains useful information about the driving signal in the vicinity of the avoided crossing. The bright diamond edges occur for combinations of static flux detuning δf_{dc} and rf amplitude where an extremum

of the driving wave form just reaches an avoided crossing. At these parameter values, the system spends the most time in the vicinity of the avoided crossing, thus allowing for maximum population transfer. As described below, this phenomenon allows us to use the bright bands due to transitions at a particular avoided crossing to image the extrema of an rf pulse.

In our experiment, we synthesized the control pulses digitally using the Tektronix AWG5014 arbitrary wave-form generator with effectively 250 MHz analog output bandwidth. The pulses were launched through a coaxial cable into an on-chip coplanar waveguide terminated in an “antenna” (loop of wire). The dispersive impedance of this antenna and the resistive coaxial cable, along with their associated unavoidable impedance mismatch and frequency-dependent inductive coupling to the qubit, call for amplitude and phase calibration *at the device* for each frequency component of the pulse. To demonstrate our method of pulse imaging and calibration, we drive the qubit with the biharmonic signal

$$f_{rf}(t) = A_1 \cos(\omega t + \theta) + A_2 \cos(2\omega t). \quad (1)$$

We classify the wave forms, described by Eq. (1), in terms of the relative amplitude ratio and phase between harmonic components using the notation $\{A_2/A_1, \theta\}$. The wave forms can have either two or four extrema per cycle, depending on the values A_2/A_1 and θ [see Figs. 1(c) and 1(d)].

The crossover between the domains of two and four extrema per cycle occurs at $A_2/A_1=1/4$. At this amplitude ratio, the phase $\theta=\pi$ is particularly interesting: this wave form has one parabolic (quadratic) and one flat (quartic) extremum, the flatness of which arises from the cancellation of the quadratic terms in the Taylor expansions of the two harmonic components. The presence of the flat extremum relies on the delicate balance of amplitudes and phases; hence, we exploit the $\{1/4, \pi\}$ wave form to calibrate the relative phase difference between the two frequency components at the device as shown in Fig. 2.

Each experiment uses the following pulse sequence [see Fig. 1(a)]. A static flux is applied using a superconducting coil and is fixed at some value δf_{dc} . A harmonic, 11-MHz, and 3- μ s cooling pulse initializes the qubit to its ground

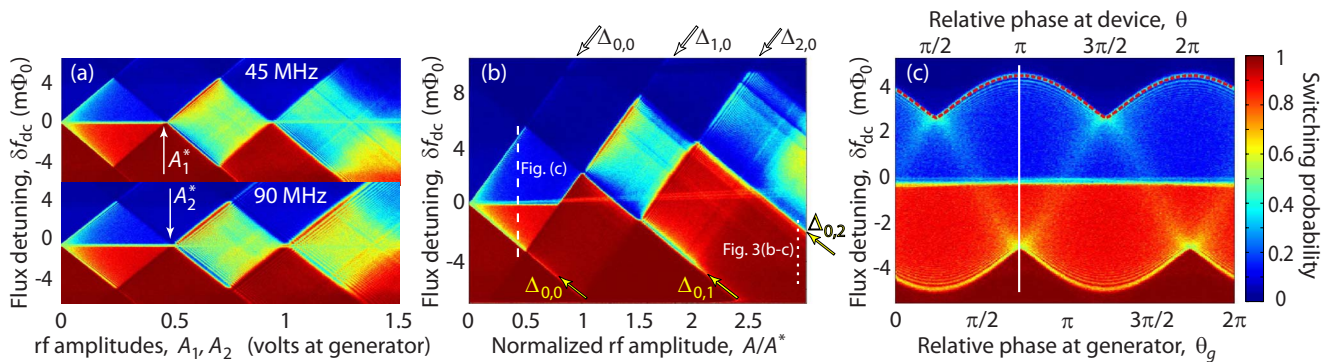


FIG. 2. (Color online) Calibration of rf amplitude and phase using long pulses. (a) Spectroscopic diamonds from single-harmonic driving. The points $A_{1,2}^*$ of optimal cooling (arrows) are used for amplitude calibration at each frequency. (b) Diamonds when driving with the biharmonic wave form $\{1/4, \pi\}$ at $\omega/2\pi=45$ MHz [see Eq. (1)]. The arrows point out the diamond edges corresponding to the quartic extremum reaching the $\Delta_{0,q}$ crossings and the quadratic reaching $\Delta_{p,0}$. (c) Measurement along the dashed line in (b) for varying θ_g . The quartic extremum $\theta=\pi$ is obtained at a cusp (solid white line) [cf. Fig. 1(d)].

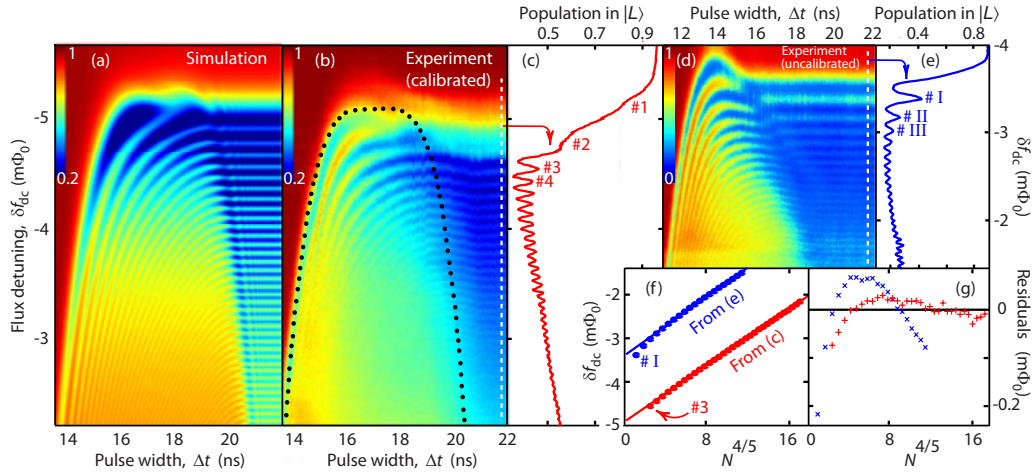


FIG. 3. (Color online) Time-dependent response. (a),(b) Population in state $|L\rangle$ at the final time Δt of a variable-length flattop pulse $\{1/4, \pi\}$, reaching through $\Delta_{0,2}$ as in Fig. 1(b). The amplitude A is indicated by the rightmost dotted line in Fig. 2(b). The edges of the curved fringes provide a direct image of the pulse (black dotted line), obtained experimentally by comparing (a) and (b). (c) Population in state $|L\rangle$ after a return trip ($\Delta t=22$ ns) through $\Delta_{0,2}$. (d),(e) Like (b) and (c) but with a wave form calibrated using the long pulses in Fig. 2, thus failing to give the correct wave form. (f) The lower (red) and upper (blue) sets of data show the spacings of the Stückelberg-interference fringes in (c) and (e), respectively, with fits to the $N^{4/5}$ power law (fringes $N=4-35$ and III-XXI fitted). (g) The residuals indicate that the fringes in (e) (blue \times) do not fit well, while those in (c) (red $+$) fit better; this confirms that the calibrated pulse better approximates the $\{1/4, \pi\}$ wave form.

state.²⁰ After a short delay (~ 20 ns), an rf-driving pulse of duration Δt and amplitude f_{rf} is applied. The mixer in Fig. 1(a) is used to terminate the pulse after a time Δt in the experiments shown in Figs. 3(b) and 3(d), but is not used in the experiments of Fig. 2. After another short delay, a sample-and-hold current pulse is applied to the hysteretic superconducting quantum interference device (SQUID) magnetometer,²¹ which measures the qubit in the basis of the diabatic states, and is set to switch only if the qubit is in state $|L\rangle$. The resulting voltage signal is amplified at room temperature and recorded with a threshold detector. This sequence is repeated a few thousand times at a rate of 10 kHz.

First, we independently calibrate the amplitudes of the two components 1 and 2 by finding their points of optimal cooling²⁰ in a single-frequency spectroscopy diamond [see Fig. 2(a)]. These points occur when the flux excursion precisely reaches both opposite side-avoided crossings $\Delta_{0,1}$ and $\Delta_{1,0}$ at zero dc bias. We denote these amplitudes by $A_{1,2}^*$ and define $A^*=A_1^*+A_2^*$ and $A=A_1+A_2$. By adding the two harmonics together, fixing the amplitude at a value within the range $0 < A/A^* < 0.5$ [see Fig. 2(b), dashed line], and scanning over flux detuning δf_{dc} and phase θ_g at the generator, we obtain Fig. 2(c). As mentioned above, high intensity occurs when an extremum of the wave form just reaches an avoided crossing. Thus, the value of θ_g at the cusps in Fig. 2(c) corresponds to the desired value of $\theta = \pi$ at the device [cf. Fig. 1(d)].

Applying the calibrated composite $\{1/4, \pi\}$ wave form to the device, we obtained the biharmonic spectroscopy diamonds in Fig. 2(b). The diamonds are skewed compared to Fig. 2(a) due to the asymmetry of the signal $f_{\text{rf}}(t)$ about zero; a quadratic extremum has a larger amplitude than a quartic. Additionally, the data exhibit greatly enhanced population transfer at the diamond edges arising from the flat extremum relative to that at the edges arising from the parabolic extre-

num; the same is seen at the cusps in Fig. 2(c). As discussed above, the reason is that the flat maximum makes the system spend more time at the avoided crossing than does the parabolic maximum.

The data in Fig. 2 reflect the averaged response of the qubit after a $3\text{-}\mu\text{s}$ pulse of base frequency $\omega/2\pi=45$ MHz (135 cycles). However, on short time scales, the pulse requires a few cycles to reach its steady-state amplitude, attributable to the buildup time of the standing-wave voltage at the imperfectly terminated end of the microwave line. In order to adjust the pulse shape for short pulses, we investigate the brief temporal Larmor-type oscillations induced by a single nonadiabatic $\Delta_{0,2}$ passage, and the buildup of Stückelberg oscillations occurring during the first return trip through that crossing.

When the system traverses the crossing, the LZ process creates a quantum superposition of the states associated with different wells. Upon return, these two components interfere with the relative phase^{13,14,17}

$$\Delta\phi_{12} = \frac{1}{\hbar} \int_{t_1}^{t_2} dt \Delta\varepsilon(t), \quad (2)$$

where $\Delta\varepsilon(t)$ is the instantaneous diabatic energy-level separation. This leads to Stückelberg-interference fringes in the occupation probabilities, provided that the time of the excursion—typically a fraction of the driving period—is smaller than the relevant decoherence times.¹⁷

We apply a nominally flattop pulse with an amplitude that reaches through $\Delta_{0,2}$. At a time Δt , we abruptly terminate the pulse, and so obtain a snapshot recording of the population [see Fig. 3(b)]. Experimentally this is done in the following way. A microwave cooling pulse initializes the system to the ground state $|0, L\rangle$ at $\delta f_{\text{dc}} < 0$. Then, a biharmonic pulse (1) starts the flux excursion toward the left, drawing the system

deep into its ground state, as shown by the arrows in Fig. 1(b) (in this way we minimize the effects of unavoidable transients associated with the pulse turn-on). Upon return toward the right, the system rapidly traverses the avoided crossings $\Delta_{0,0}$ and $\Delta_{0,1}$ before reaching $\Delta_{0,2}$.²² We interrupt the excursion at the time Δt by mixing the pulse with the falling edge of a square pulse, thus returning the flux detuning to the value δf_{dc} . The population can then be read out well before interwell relaxation occurs.

For pulse lengths Δt long enough for the system to complete a round trip through $\Delta_{0,2}$, the final populations in the left and right wells are stationary, i.e., independent of Δt . The spacings of the resulting horizontal Stückelberg-interference fringes in Fig. 3(c) are determined by the phase (2) gained over the course of the excursion beyond $\Delta_{0,2}$; as described below, these fringes thus constitute a signature of the part of the wave form extending beyond the avoided crossing.

The quantization condition for interference, $\Delta\phi_{12}=2\pi N$, gives the static flux detuning $\delta f_{dc}^{(N)}$ for the N th node of constructive interference. For generic pulses with extrema that can be fit to parabolas, Eq. (2) leads to an $N^{2/3}$ power law for the values of dc-flux detuning at the interference nodes.¹⁶ However, for the $\{1/4, \pi\}$ flat-top wave form that we seek, the quartic extremum gives rise to an $N^{4/5}$ power law, which is the signature we use to determine when the desired pulse has been attained. In Figs. 3(f) and 3(g) we demonstrate the $N^{4/5}$ power law for a pulse that is calibrated by comparison to a simulation, in which we numerically integrate the Schrödinger equation for a two-level system with time-dependent driving (1). The initial state is taken to be the ground state of the system at detuning δf_{dc} . For further details, see Ref. 16. Overall there is a good agreement between simulation and experimental data. We attribute the discrepancy around $\Delta t=18$ ns, $\delta f_{dc}=-5$ m Φ_0 in Fig. 3(b) to non-

ideal pulse turn-off, and the loss of fringe contrast to intrawell relaxation, digital noise, and phase jitter.¹⁶

We note that a rectangular-pulse wave form would ideally lead to a very different fringe pattern compared to the one in Fig. 3, showing maximal contrast when the pulse height matches the level-crossing position in energy and symmetrically decreasing at higher and lower pulse amplitudes. Interestingly, in the pioneering work of Nakamura *et al.*,⁹ where such pulses were used to drive a qubit, the observed fringe pattern had a strong asymmetry, overall resembling the data in Fig. 3. This behavior can be attributed to a smooth turn-on and -off of the pulses used in that work.

In this work, we present an approach that in principle can be used to design an arbitrary wave form at the device, and we use it to drive a superconducting qubit. This technique, which is demonstrated with biharmonic driving, relies on calibrating the different Fourier harmonics comprising the wave form. Having performed such a calibration, we are able to control the time spent by the qubit near an avoided crossing. The details of qubit response are accounted for by comparison with a simulation.

We gratefully acknowledge discussions with and support from T. P. Orlando. We thank Y. Nakamura, F. Nori, and T. Yamamoto for helpful discussions and G. Fitch, V. Bolkhovskiy, P. Murphy, E. Macedo, D. Baker, and T. Weir at MIT Lincoln Laboratory for technical assistance. This work was sponsored by the U.S. Government and the W. M. Keck Foundation Center for Extreme Quantum Information Theory. M.S.R. was supported by DOE CSGF, Grant No. DE-FG02-97ER25308, and the NSF. The work at Lincoln Laboratory was sponsored by the AFOSR under Air Force Contract No. FA8721-05-C-0002.

*bylander@mit.edu

†Present address: ICREA and CIN2 ICN/CSIC, Barcelona, Spain.

‡Present address: EECS Department, MIT, Cambridge, MA, USA.

¹J. Clarke and F. K. Wilhelm, *Nature (London)* **453**, 1031 (2008).

²R. Hanson and D. D. Awschalom, *Nature (London)* **453**, 1043 (2008).

³Y. Nakamura, Y. A. Pashkin, and J. S. Tsai, *Phys. Rev. Lett.* **87**, 246601 (2001).

⁴D. Vion *et al.*, *Science* **296**, 886 (2002).

⁵J. M. Martinis, S. Nam, J. Aumentado, and C. Urbina, *Phys. Rev. Lett.* **89**, 117901 (2002).

⁶I. Chiorescu, Y. Nakamura, C. J. P. M. Harmans, and J. E. Mooij, *Science* **299**, 1869 (2003).

⁷M. Steffen, J. M. Martinis, and I. L. Chuang, *Phys. Rev. B* **68**, 224518 (2003).

⁸E. Lucero, M. Hofheinz, M. Ansmann, R. C. Bialczak, N. Katz, M. Neeley, A. D. O'Connell, H. Wang, A. N. Cleland, and J. M. Martinis, *Phys. Rev. Lett.* **100**, 247001 (2008).

⁹Y. Nakamura, Y. A. Pashkin, and J. S. Tsai, *Nature (London)* **398**, 786 (1999).

¹⁰T. Duty, D. Gunnarsson, K. Bladh, and P. Delsing, *Phys. Rev. B*

69, 140503(R) (2004).

¹¹S. Poletto *et al.*, *New J. Phys.* **11**, 013009 (2009).

¹²A. Izmalkov *et al.*, *EPL* **65**, 844 (2004).

¹³W. D. Oliver *et al.*, *Science* **310**, 1653 (2005).

¹⁴M. Sillanpää, T. Lehtinen, A. Paila, Y. Makhlin, and P. Hakonen, *Phys. Rev. Lett.* **96**, 187002 (2006).

¹⁵C. M. Wilson, T. Duty, F. Persson, M. Sandberg, G. Johansson, and P. Delsing, *Phys. Rev. Lett.* **98**, 257003 (2007).

¹⁶D. M. Berns *et al.*, *Nature (London)* **455**, 51 (2008).

¹⁷A. V. Shytov, D. A. Ivanov, and M. V. Feigel'man, *Eur. Phys. J. B* **36**, 263 (2003).

¹⁸S. Ashhab, J. R. Johansson, A. M. Zagoskin, and F. Nori, *Phys. Rev. A* **75**, 063414 (2007).

¹⁹E. M. Fortunato *et al.*, *J. Chem. Phys.* **116**, 7599 (2002).

²⁰S. O. Valenzuela *et al.*, *Science* **314**, 1589 (2006).

²¹*The SQUID Handbook: Fundamentals and Technology of SQUIDS and SQUID Systems*, edited by J. Clarke and A. I. Braginski (Wiley, Weinheim, 2004), Vol. I.

²²Because $\Delta_{0,0}, \Delta_{0,1} \ll \Delta_{0,2}$, the population change over 1 cycle is dominated by LZ transitions at $\Delta_{0,2}$.